AGU PUBLICATIONS

JGR

Journal of Geophysical Research: Space Physics

RESEARCH ARTICLE
10.1002/2015JA021911

Data-driven modeling of the solar wind from 1 R_s to 1 AU

Xueshang Feng[1], Xiaopeng Ma[1,2], and Changqing Xiang[1]

[1] SIGMA Weather Group, State Key Laboratory for Space Weather, National Space Science Center, Chinese Academy of Sciences, Beijing, China, [2] College of Earth Sciences, Graduate University of Chinese Academy of Sciences, Beijing, China

Key Points:
- Use the consecutive high-cadence GONG's magnetogram synoptic maps as input
- Continuously drive the model at the solar surface by the characteristic method
- Trace the evolution of the global coronal response to variations of the photospheric magnetic field

Correspondence to:
X. Feng,
fengx@spaceweather.ac.cn

Citation:
Feng, X., X. Ma, and C. Xiang (2015), Data-driven modeling of the solar wind from 1 R_s to 1 AU, *J. Geophys. Res. Space Physics*, *120*, 10,159–10,174, doi:10.1002/2015JA021911.

Received 13 SEP 2015
Accepted 16 NOV 2015
Accepted article online 20 NOV 2015
Published online 9 DEC 2015

Abstract We present here a time-dependent three-dimensional magnetohydrodynamic (MHD) solar wind simulation from the solar surface to the Earth's orbit driven by time-varying line-of-sight solar magnetic field data. The simulation is based on the three-dimensional (3-D) solar-interplanetary (SIP) adaptive mesh refinement (AMR) space-time conservation element and solution element (CESE) MHD (SIP-AMR-CESE MHD) model. In this simulation, we first achieve the initial solar wind background with the time-relaxation method by inputting a potential field obtained from the synoptic photospheric magnetic field and then generate the time-evolving solar wind by advancing the initial 3-D solar wind background with continuously varying photospheric magnetic field. The model updates the inner boundary conditions by using the projected normal characteristic method, inputting the high-cadence photospheric magnetic field data corrected by solar differential rotation, and limiting the mass flux escaping from the solar photosphere. We investigate the solar wind evolution from 1 July to 11 August 2008 with the model driven by the consecutive synoptic maps from the Global Oscillation Network Group. We compare the numerical results with the previous studies on the solar wind, the solar coronal observations from the Extreme ultraviolet Imaging Telescope board on Solar and Heliospheric Observatory, and the measurements from OMNI at 1 astronomical unit (AU). Comparisons show that the present data-driven MHD model's results have overall good agreement with the large-scale dynamical coronal and interplanetary structures, including the sizes and distributions of the coronal holes, the positions and shapes of the streamer belts, the heliocentric distances of the Alfvénic surface, and the transitions of the solar wind speeds. However, the model fails to capture the small-sized equatorial holes, and the modeled solar wind near 1 AU has a somewhat higher density and weaker magnetic field strength than observed. Perhaps better preprocessing of high-cadence observed photospheric magnetic field (particularly 3-D global measurements), combined with plasma measurements and higher resolution grids, will enable the data-driven model to more accurately capture the time-dependent changes of the ambient solar wind for further improvements. In addition, other measures may also be needed when the model is employed in the period of high solar activity.

1. Introduction

Numerical space weather modeling plays an important role in space weather studies. Three-dimensional numerical magnetohydrodynamic (MHD) modeling can achieve a first approximation to the complicated physics by providing a simplified description of natural phenomena in space plasmas. MHD models enable us to reproduce space weather conditions and help us to understand some of their related physical processes [*Dryer*, 2007; *Aschwanden et al.*, 2008; *Watermann et al.*, 2009; *Feng et al.*, 2011a, 2013]. For such purpose, some MHD models have been developed [e.g., *Usmanov and Goldstein*, 2006; *Feng et al.*, 2010; *Nakamizo et al.*, 2009; *Riley et al.*, 2011; *Tóth et al.*, 2012; *Hayashi*, 2013]. As an essential part of space weather predictions, the study of steady solar wind is of great importance. On the one hand, some large-scale structures in the solar wind background may cause adverse effects in the geospace [*Gonzalez et al.*, 1989; *Tsurutani et al.*, 2006]. On the other hand, in modeling the evolution of coronal mass ejections (CMEs) in the heliosphere, the quasi-steady solar wind serves as the initial state, on which modelers impose various mimicked eruption models, such as flux rope models [*Wu et al.*, 1999; *Tóth et al.*, 2007; *Manchester et al.*, 2008; *Lugaz et al.*, 2011; *Lionello et al.*, 2013; *Zhou and Feng*, 2013; *Zhou et al.*, 2014], the cone model [*Zhao et al.*, 2002; *Xie et al.*, 2004; *Wu et al.*, 2007], and the shock jump conditions [*van der Holst et al.*, 2005].

Physically speaking, photospheric magnetic field dominates solar coronal states and thus controls the heliospheric large-scale solar wind structures [*Mikić et al.*, 1999; *Neugebauer et al.*, 1998; *Mackay and van Ballegooijen*, 2006]. Global estimates of the solar photospheric magnetic field distribution are critical for most

numerical solar wind modeling efforts. Most current MHD models for the solar wind from the Sun to Earth usually initialize the codes by using potential magnetic field based on the synoptic charts of the photospheric magnetic field and Parker solar wind solution to obtain a steady-state equilibrium with time-relaxation methods [e.g., *Hayashi*, 2005; *Usmanov and Goldstein*, 2006; *van der Holst et al.*, 2010; *Tóth et al.*, 2012; *Feng et al.*, 2014a, 2014b]. For comparative analyses of current three-dimensional numerical solar wind models, the readers may refer to *Wu and Dryer* [2015]. Alternatively, a 3-D iterative tomography, which modifies a time-dependent three-dimensional kinematic heliospheric model to fit interplanetary scintillation (IPS) observations, can supply solar wind velocity and density from 15 R_s to 3 AU [*Jackson et al.*, 2011; *Jian et al.*, 2015]. This 3-D tomography technique can also be combined with some magnetic field models based on photospheric magnetograms to specify the bottom boundary conditions for the MHD solar wind simulations [*Yu et al.*, 2015; *Jackson et al.*, 2015].

Synoptic maps of solar photospheric magnetic field are constructed by combining all the values for each Carrington longitude from line of sight (LOS) photospheric magnetograms during the specified Carrington rotations (CRs). For each magnetogram, the data within a certain longitudinal range of the central meridian are used to create the synoptic maps. The individual values for each Carrington longitude are weighted for the central meridian distance [*Ulrich et al.*, 2002; *Liu et al.*, 2012]. Due to the LOS measurements only available from the ground stations or the instruments board on spacecraft orbiting in the ecliptic plane, there are data gaps in the polar regions of the synoptic maps because the projection effect on the LOS measurements leads to too much noise of the data in polar regions, and once a year the inclination of the elliptic plane with respect to the solar equatorial plane causes data from any one pole to be missing entirely. Several methods have been put forward to fill the polar data gaps. *Svalgaard et al.* [1978] analyzed the magnetograms at Wilcox Solar Observatory (WSO) and concluded that the magnetic field poleward 55° latitude was nearly radial and of the form 11.5 $\cos^8\theta$ (where θ is colatitude) during 1976–1977. *Wang and Sheeley* [1992] developed potential models of solar corona by using similar formulae to extrapolate the polar field. *Arge and Pizzo* [2000] filled the polar field by fitting a second-order polynomial to the most reliable observations, which were made when the absolute values of solar *b* angles were greater than 5°. Using the data from Solar and Heliospheric Observatory (SOHO)/Michelson Doppler Imager, *Liu et al.* [2007] compared the performances of interpolating the polar fields with the following seven methods: one-dimensional (1-D) cubic spline interpolation method, the potential field method, the smoothed 1-D cubic spline interpolation method, the method of *Svalgaard et al.* [1978], the two-dimensional (2-D) temporal interpolation method, the 2-D spatial interpolation method, and the flux transport model based method [*Schrijver et al.*, 2002]. *Sun et al.* [2011] developed a new technique by combining a two-dimensional spatial/temporal interpolation and a simple version of the flux transport model.

When the full rotation synoptic maps of photospheric field are used to constrain the solar wind model, the solar magnetic field is assumed to change very little during a CR. This assumption is rather reasonable during solar minimum phases. However, the solar magnetic field varies dramatically especially near solar maxima and in ascending phases [*Smith et al.*, 2001; *Burlaga et al.*, 2002; *Goelzer et al.*, 2013]. The steady solar wind prescribed by the full rotation synoptic maps can basically capture some global structures, but they can hardly reproduce the dynamic features in the solar corona and heliosphere [e.g., *Usmanov and Goldstein*, 2006; *van der Holst et al.*, 2010; *Feng et al.*, 2011b; *Tóth et al.*, 2012]. In order to better determine background solar wind changes, researchers advanced their simulation using daily-updated synoptic maps of the photospheric magnetic field instead of the full rotation synoptic maps. The advantage of a daily-updated map (over a full rotation map) lies in that part of the map directed toward the Earth consists of the most recent magnetic observations available. *Arge and Pizzo* [2000] input the daily-updated synoptic maps into the Wang-Sheele-Arge (WSA) model and improved the prediction of the solar wind conditions with a continuous empirical function. *Hayashi* [2013] applied the temporally varying solar radial magnetic field to the time-dependent solar wind MHD model, which can trace the evolution of the global solar coronal response to variations of the photospheric magnetic field. *Intriligator et al.* [2012] combined the WSA model with the daily-updated synoptic maps to achieve the inner boundary at 0.1 AU for the model of hybrid heliospheric modeling system with pickup protons. In addition, *Hernández et al.* [2007] incorporated the data of farside active regions derived from helioseismology into the daily-updated data. Besides, *Yang et al.* [2012] drove the SIP-AMR-CESE MHD model with daily-updated synoptic magnetograms of WSO to study the dynamic evolution of the global corona.

It is well known that solar differential rotation causes its surface to spin at different rates as measured by motions of structures on the photosphere. However, the synoptic maps of photospheric magnetic field

generated above are generally based on the premise that the photosphere rotates rigidly at different latitudes, so they contain no information on the solar differential rotation. Recent studies began to take into account of the solar differential rotation when considering the distribution of photospheric magnetic field. *Arge et al.* [2013] and *Hickmann et al.* [2015] produced realistic estimates of the instantaneous global photospheric magnetic field distribution by using the Air Force Data Assimilative Photospheric Flux Transport model, which can assimilate helioseismic farside active region data and the evolved magnetic flux when the observation is not available. *Lionello et al.* [2005] used a global 3-D MHD model to study the effects of differential rotation on the coronal magnetic field by introducing an artificial differential rotation into a steady corona solution obtained from the time-relaxation method. They identified examples of interchange reconnection and found other changes of the magnetic field topology due to the differential rotation. *Yeates et al.* [2007] corrected the synoptic maps with solar differential rotation and employed the corrected data to initialize the surface flux transport model [*Wang et al.*, 1989, 2002]. Using the same method, *Feng et al.* [2012a] produced the global time-varying and self-consistent synchronic snapshots of the photospheric magnetic field to advance the 3-D numerical global SIP-AMR-CESE-MHD model. *Zhao et al.* [2004] proposed a modified version of synoptic charts, named a "synchronic frame", in which the positions of the synoptic data are longitudinally shifted in accordance with the solar differential rotation. The synchronic frame data of photospheric magnetic field have been used by *Hayashi et al.* [2008] in simulating the global solar corona around the Halloween event in 2003.

Global simulation of dynamic solar wind is one of the most challenging problems in space weather modeling. Solar wind is rather than of steady state but physically dynamic corresponding to the solar rotation, solar mass flow, and solar magnetic field evolution, especially during solar eruptions [*Tu and Marsch*, 1995; *Zurbuchen and Richardson*, 2006; *McComas et al.*, 2008]. As mentioned above, some solar wind simulations have been performed to reproduce the time-varying structures of solar wind. However, modelers should be very cautious to utilize the daily-updated or higher-cadence synoptic maps to drive the solar wind simulations. These synoptic maps usually contain too much noise and very strong magnetic field in active regions. A proper smoothing procedure is needed to make the photospheric magnetic map friendly as input to MHD models. In addition, the synoptic maps can serve as the near-realistic inner boundary conditions for the radial magnetic field of solar corona. However, updating the radial magnetic field by employing the synoptic maps without special care probably leads to the physical inconsistency and the unphysical oscillations near the sub-Alfvénic solar surface boundary [*Nakagawa*, 1980, 1981a, 1981b; *Wang et al.*, 1982]. In order to minimize these effects, researchers [*Wu et al.*, 2006; *Wang et al.*, 2011; *Feng et al.*, 2012a; *Hayashi*, 2012, 2013] prescribed the inner boundary conditions using the projected normal characteristic (PNC) method developed by *Nakagawa* [1980, 1981a, 1981b], *Wang et al.* [1982], and *Nakagawa et al.* [1987]. Inspired by *Mikić et al.* [1999], *Yang et al.* [2012], and *Feng et al.* [2012c] solved a Poisson equation on the spherical surface at 1 solar radius (R_s) to deal with the nonzero tangential electric field due to the varying radial magnetic field so that the photospheric synoptic maps can be self-consistently combined with the PNC method at the inner boundary.

Based on the above considerations, we devote our data-driven SIP-CESE-MHD model to simulating the temporal solar wind evolution from 1 July to 11 August in 2008 by using 6 h cadence synoptic maps provided by Global Oscillation Network Group (GONG). The code first achieves a steady-state equilibrium of solar wind using the above-mentioned preprocessed synoptic map on 1 July. Based on the simulated background solar wind, we then advance our model with the changing bottom boundary, which is determined from the PNC method and the continuously time-varying solar observations. Finally, we achieve the temporally varying solar wind structures in response to the changing photospheric magnetic field.

This paper is organized as follows. In section 2, we briefly describe the main aspects of the SIP-CESE-MHD model. Section 3 lists the processing methods of synoptic maps and the treatments of boundary conditions. In section 4, we present the simulation results and compare them with the SOHO/Extreme ultraviolet Imaging Telescope (EIT) observations and the OMNI data at 1 AU. Finally, some concluding remarks and discussions are made in the last section.

2. Model Description

The three-dimensional MHD equations governing solar wind plasma used in this work are written as:

$$\frac{\partial \mathbf{U}}{\partial t} + \nabla \cdot \mathbf{F} = \mathbf{S}, \tag{1}$$

where

$$\mathbf{U} = \left(\rho, \rho\mathbf{v}, e_1, \mathbf{B}_1\right)^T,$$

$$\mathbf{F} = \begin{pmatrix} \rho\mathbf{v} \\ \rho\mathbf{v}\mathbf{v} + \mathbf{I}\left(p + \frac{1}{2}\mathbf{B}_1^2 + \mathbf{B}_1 \cdot \mathbf{B}_0\right) - \mathbf{B}_1\mathbf{B}_1 - \mathbf{B}_1\mathbf{B}_0 - \mathbf{B}_0\mathbf{B}_1 \\ \mathbf{v}(e_1 + p + \frac{1}{2}\mathbf{B}_1^2 + \mathbf{B}_1 \cdot \mathbf{B}_0) - (\mathbf{v} \cdot \mathbf{B}_1)(\mathbf{B}_1 + \mathbf{B}_0) \\ \mathbf{v}\mathbf{B} - \mathbf{B}\mathbf{u} \end{pmatrix},$$

and

$$\mathbf{S} = [0, \mathbf{F}_0, \mathbf{v} \cdot \mathbf{F}_0, \mathbf{0}]^T - \nabla \cdot \mathbf{B}(0, \mathbf{B}, \mathbf{v} \cdot \mathbf{B}, \mathbf{v})^T + \mathbf{S}_H,$$

with $e_1 = \frac{p}{\gamma-1} + \frac{1}{2}\rho\mathbf{v}^2 + \frac{1}{2}\mathbf{B}_1^2$. Here ρ, $\mathbf{v}$, p, and $\mathbf{B}$ are the mass density, plasma velocity, gas pressure, and magnetic field, respectively. The external force exerted on the plasma $\mathbf{F}_0 = -\frac{GM_s}{r^3}\mathbf{r} - \boldsymbol{\Omega} \times \boldsymbol{\Omega} \times \mathbf{r} - 2\boldsymbol{\Omega} \times \mathbf{v}$ is the sum of solar gravity force and inertial force in the corotating frame with the Sun. $G = 6.67384 \times 10^{-11}$ m^{3}kg^{-1}s^{-2}, $M_s = 1.989 \times 10^{30}$kg, and $\Omega = 13.2$ deg/day, which stand for the gravity constant, the mass of the Sun, and the angular speed of solar rotation, respectively.

In the MHD model, the Powell's source terms $-\nabla \cdot \mathbf{B}(0, \mathbf{B}, \mathbf{v} \cdot \mathbf{B}, \mathbf{v})^T$ are added to advect the divergence of magnetic field $\nabla \cdot \mathbf{B}$ with the velocity of the plasma flow [*Powell et al.*, 1999; *Tóth et al.*, 2006]. Besides, the magnetic field is split into two parts $\mathbf{B} = \mathbf{B}_0 + \mathbf{B}_1$ [*Tanaka*, 1994; *Gombosi et al.*, 2003; *Nakamizo et al.*, 2009; *Feng et al.*, 2010], where $\mathbf{B}_0$ represents the time-independent potential magnetic field calculated from the initial synoptic maps and $\mathbf{B}_1$ is the time-dependent part updated by the MHD solver. This technique can make the MHD solver numerically less challenging to maintain positive pressure [*van der Holst et al.*, 2010; *Janhunen et al.*, 2012; *Tóth et al.*, 2012; *Feng et al.*, 2014a, 2014b].

In solar wind simulation, coronal heating/solar acceleration plays an important role in producing realistic solar wind solution. Various empirical heating terms [*Mikić et al.*, 1999; *Usmanov et al.*, 2000; *Roussev et al.*, 2003; *Cohen et al.*, 2008; *Nakamizo et al.*, 2009; *Feng et al.*, 2010; *van der Holst et al.*, 2010; *Riley et al.*, 2011] are usually added to the MHD equations to achieve the observed pattern of fast and slow solar wind. In this paper, following *Feng et al.* [2010], the volume heating source terms are expressed in the form of $\mathbf{S}_H = \left(0, S_M\mathbf{e}_r, S_E, \mathbf{0}\right)^T$, where $S_M = Q_M C_a \left(\frac{r}{R_s} - 1\right) \exp\left(-\frac{r}{L_M}\right)$ and $S_E = Q_1 C_a \exp\left(-\frac{r}{L_{Q_1}}\right) + Q_2 C_a \left(\frac{r}{R_s} - 1\right) \exp\left(-\frac{r}{L_{Q_2}}\right)$. Here L_M, L_{Q_1}, and L_{Q_2}, heating heights, are set to be 1 R_s, 0.8 R_s, and 1 R_s. The coefficients Q_M, Q_1, and Q_2 are 7.9×10^{-14}Nm^{-3}, 1.18×10^{-7}Jm^{-3}s^{-1}, and 1.5×10^{-9}Jm^{-3}s^{-1}, respectively. Besides, $C_a = C_a' / \max(C_a')$ is a normalized profile factor closely related to the Wang-Sheeley-Arge (WSA) model [*Wang et al.*, 1997; *Arge and Pizzo*, 2000; *Arge et al.*, 2003, 2004; *Owens et al.*, 2005], with $C_a' = \frac{(5.8 - 1.6e^{[1-(\theta_b/8.5)^3]})^{3.5}}{(1+f_s)^{2/7}}$. f_s, the magnetic field expansion factor, reads $f_s = \left(\frac{1}{R}\right)^2 \frac{B_{R_s}}{B_R}$, where B_{R_s} and B_R are the magnetic field strength at the solar surface and at the heliocentric distance $R = 2.5$ R_s . θ_b is the angular distance of the particular field line from the nearest coronal hole boundary.

In solving the MHD equations, if the magnetic field is very strong, the total energy is dominated by magnetic energy, which may result in negative thermal pressures when subtracting the magnetic energy from the total energy. In order to avoid this, we solve the following pressure equation,

$$\frac{\partial p}{\partial t} + \nabla \cdot (\mathbf{v}p) = -(\gamma - 1)p\nabla \cdot \mathbf{v} + (\gamma - 1)S_E$$

directly instead of the energy equation. In program coding, we employ the switch designed by *Balsara and Spicer* [1999] to detect the grid points where the negative pressures may occur and solve the pressure equation only on these points. If negative pressures still occur, we either replace them with the positive ones of the previous time step.

The governing equation (1) of solar wind plasma and magnetic field are solved by our SIP-CESE-MHD solver in an AMR six component grid [*Feng et al.*, 2010, 2012a, 2013, 2014b]. The whole grid is decomposed into six identical components, and each component is a part of low-latitude spherical grid. The SIP-CESE solver was developed in a series of articles [*Feng et al.*, 2007, 2010] and validated for MHD equations in general coordinates by *Feng et al.* [2012a]. The grid and solver are implemented in the parallelized Adaptive Mesh Refinement

code of PARAMESH [*MacNeice et al.*, 2000]), which provides friendly interfaces to parallelize serial code in the Cartesian grid with the AMR feature, and can also be applied to the curvilinear grid with proper treatments for coordinate transformation.

In the simulation, the computational domain extends from 1 R_s to 256 R_s, and each component consists of $14 \times 4 \times 4$ blocks. Each block is an $8 \times 8 \times 8$ cubic grid in a reference space (λ, θ, ϕ), where $\lambda = \ln r$ and (r, θ, ϕ) are the spherical coordinates. The grid near the current sheet is refined at most 4 times which makes the grid spacings become 1/16 of the original ones. The MHD variables are initiated with Parker solar wind solution and magnetic field calculated from the potential field. After adequate time of relaxation, the solution given by the SIP-CESE-MHD solver tends to be steady. Once the equilibrium state of solar wind is achieved, we start to apply time-dependent boundary conditions to investigate the dynamic corona and interplanetary structures in response to the time-evolving photospheric magnetic field.

3. Data Preprocessing and Boundary Conditions

In this section, we focus our attention on how to generate the time-varying magnetic field data to drive the model according to the standard magnetogram synoptic maps available from GONG at http://gong.nso.edu/data/magmap/QR/bqs/ and how to combine them with the PNC method.

3.1. Magnetic Synoptic Data Preprocessing

We choose the synoptic map data of photospheric magnetic field as the input to the SIP-CESE-MHD model based on the following considerations. First, the GONG network is comprised of six solar observatories at different longitudes of the Earth to make 24 h a day observations of the Sun [*Hill et al.*, 1994a, 1994b; *Harvey et al.*, 1996], which enables the GONG network to provide 6 h cadence synoptic maps in 2008. Second, it uses the Ni I line at 676.8 nm in the solar spectrum to measure the LOS photospheric field strength. Comparing with the observations using the Fe I 523.3 nm line (e.g., WSO), the data do not need to be corrected due to the saturation effects [*Ulrich*, 1992; *Arge et al.*, 2002]. Finally, polar fields not well-observed have been represented by a cubic polynomial surface fit to the observed fields at neighboring latitudes.

The 6-hourly updated synoptic maps of photospheric magnetograms must be preprocessed before they are input into the SIP-CESE-MHD model. We first synchronize all the data points to the observation time of the magnetograms at the central meridian by taking the solar differential rotation into consideration. For a data point at the Carrington longitude ϕ_0 and colatitude θ on the 6-hourly updated synoptic map, the new longitude ϕ on the corrected map is given by *Yeates et al.* [2007]. The derived relationship between ϕ and ϕ_0 reads

$$\phi_0 = \frac{\Omega\left(\phi - \phi_{\text{ref}}\right)}{\Omega' + \Omega} + \phi_{\text{ref}}.$$

Here ϕ_{ref} is the Carrington longitude of the central meridian on the 6-hourly updated synoptic map of GONG. Ω is the rotation rate of the Carrington frame with respect to an observer on the Earth and has the value of 13.2 deg/day. Ω' is the angular velocity of solar differential rotation, for which we use the formula presented by *Snodgrass* [1983],

$$\Omega' = 0.18 - 2.3\cos^2\theta - 1.62\cos^4\theta.$$

Then the magnetic field at (θ, ϕ) is interpolated from the original synoptic map according to the coordinates (θ, ϕ_0). It should be mentioned that the longitude ϕ may exceed the left or right edge of the original map, and thus, we have to use three neighboring synoptic maps to generate one corrected map.

In order to be consistent with the corotating frame used in SIP-CESE-MHD model, all the synoptic maps corrected above are adjusted by shifting the meridian at the Carrington longitude of 360°to their left edges, so that their initial Carrington longitudes are aligned. As we know, it is the photospheric magnetic field that the synoptic maps record. In order to accommodate the synoptic maps to the model's bottom boundary on the solar surface, a Gaussian-smooth procedure [*Hayashi*, 2013] is applied to reduce the noise, which makes the photospheric magnetic maps much easier to be dealt with by the MHD solver. Finally, the magnetic monopoles are removed by subtracting the excess global magnetic flux from the smoothed synoptic maps. For convenience of later use, we use the word "processed" to mean the 6-hourly updated synoptic map from GONG after the above preprocessing procedures.

The time steps of SIP-CESE-MHD model on the solar surface are much smaller than the 6 h cadence of synoptic maps. To fill the gaps between two neighboring processed synoptic maps, we apply a three-order Lagrange-interpolation over time. For any specified time t, we first find three consecutive maps $B_{r,1}$, $B_{r,2}$, and $B_{r,3}$ on the condition that their observation time t_1, t_2, and t_3 are nearest to t among all the processed maps. Then the radial magnetic field on the solar surface at time t can be interpolated by

$$B_r(t) = \frac{(t-t_2)(t-t_3)}{(t_1-t_2)(t_1-t_3)}B_{r,1} + \frac{(t-t_1)(t-t_3)}{(t_2-t_1)(t_2-t_3)}B_{r,2} + \frac{(t-t_1)(t-t_2)}{(t_3-t_1)(t_3-t_2)}B_{r,3}.$$

The interpolated synoptic maps converge to the processed ones every 6 h. As a result, this method does not lose time accuracy due to the long-term simulation.

3.2. Projected Normal Characteristic Boundary Condtions

With the radial magnetic field B_r given by synoptic maps, we use the PNC method plus the plasma mass flux limit to prescribe the eight variables on the solar surface. This method was described [*Hayashi*, 2005; *Yang et al.*, 2012; *Feng et al.*, 2012b] in detail. However, it needs further treatment when applied to our situation because $\frac{\partial B_r}{\partial t}$ is no longer zero in our simulation.

According to the discussion given by *Mikić et al.* [1999] and *Yang et al.* [2012], we use a solenoidal field assumption of the tangential electric field, $\mathbf{E}_t$, on the solar surface. Thus, $\mathbf{E}_t = \nabla_t \times (\Psi \mathbf{e}_r)$, where Ψ is a function of θ and ϕ, and ∇_t indicates tangential derivative operator in the $\theta - \phi$ plane. Then we get $\nabla^2\Psi = \frac{\partial B_r}{\partial t}$, which can be solved by a Poisson solver and used to calculate $\mathbf{E}_t$. The subscript t stands for the tangential components of a vector on the solar surface.

Considering $\mathbf{E}_t = -(\mathbf{v} \times \mathbf{B})_t$, we have

$$\frac{\partial E_\theta}{\partial t} = B_\phi \frac{\partial v_r}{\partial t} + v_r \frac{\partial B_\phi}{\partial t} - B_r \frac{\partial v_\phi}{\partial t} - v_\phi \frac{\partial B_r}{\partial t} \tag{2}$$

and

$$\frac{\partial E_\phi}{\partial t} = B_r \frac{\partial v_\theta}{\partial t} + v_\theta \frac{\partial B_r}{\partial t} - B_\theta \frac{\partial v_r}{\partial t} - v_r \frac{\partial B_\theta}{\partial t}, \tag{3}$$

from which $\frac{\partial v_\theta}{\partial t}$ and $\frac{\partial v_\phi}{\partial t}$ can be derived and applied to the PNC method instead of $v_\phi B_r - v_r B_\phi = 0$ and $v_\theta B_r - v_r B_\theta = 0$ [*Yang et al.*, 2012]. Then we apply the limit of the plasma mass flux escaping from the solar surface and the invariant entropy to the model's inner boundary and obtain another two independent constraints on the derivatives of MHD variables [*Hayashi*, 2005; *Yang et al.*, 2012; *Feng et al.*, 2012b].

Considering $\frac{\partial B_r}{\partial t}$ from the observation, equations (2) and (3), two constraints from the plasma mass flux limit and the invariant entropy, we still need three equations to specify the bottom boundary conditions. Here we make use of three projected normal characteristic equations associated with the eigenvalues of $v_r - v_f$, $v_r - v_A$, and $v_r - v_s$, which are always negative at the inner boundary because v_r is usually small on the solar surface. The details of the related equations can be seen in Appendices of *Hayashi* [2005] and are not repeated here. As done by *Feng et al.* [2012b], these three equations are discretized by the Lax scheme [*Lax and Wendroff*, 1960]. After substituting the four constraints and $\frac{\partial B_r}{\partial t}$ into the three characteristic equations, we solve them by using the linear solver of Intel Math Kernel Library (https://software.intel.com/en-us/intel-mkl) to achieve the derivatives of all the MHD variables except B_r.

Obviously, $\frac{\partial v_\theta}{\partial t}$ and $\frac{\partial v_\phi}{\partial t}$ can be derived from equations (2) and (3) by dividing B_r. If $|B_r|$ is very small, the division will cause unacceptable errors and even make the code fail to proceed during the simulation. Thus, if $|B_r|$ is detected to be smaller than 0.1 Gauss, the magnetic field will be calculated by PFSS model, and the velocities are set to be parallel to the magnetic field. The regions affected are illustrated in Figure 1 with green color, from which we can see that only small parts of the solar surface are affected. In order to guarantee positive pressures and densities, if $\rho < \rho_{\min}$ or $p < p_{\min}$, $\frac{\partial \rho}{\partial t} = 0$ and $\frac{\partial p}{\partial t} = 0$ are strictly applied to limit their tendency to decrease. Here $\rho_{\min}$ and $p_{\min}$ are chosen to be $1.5 \times 10^7 \mathrm{cm}^{-3}$ and 10^{-4} Pa.

4. Simulation Results

Based on the data-driven SIP-CESE-MHD model described above, we simulate the evolution of the solar corona and solar wind from 1 July to 11 August 2008 by using the 6-hourly updated synoptic maps from GONG

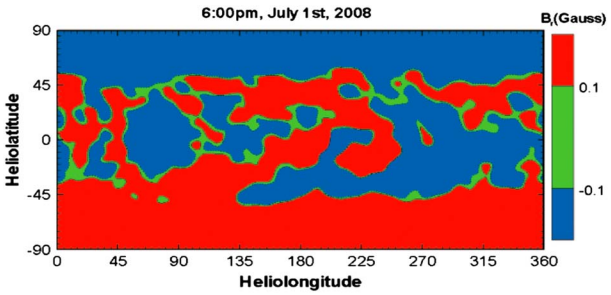

Figure 1. Illustration of the regions where $|B_r| < 0.1$ Gauss. The regions with green color are specially treated in the boundary determination instead of using the characteristic projection method.

as input. The initial solar wind is generated with the synoptic map of the photospheric magnetic field on 1 July. After the equilibrium state is achieved, the 164 consecutive preprocessed synoptic maps are applied to drive the SIP-CESE-MHD model. In the simulation, the parameters f_s and θ_b used in the volume heating coefficients are recalculated once a day. The calculations were performed on the TianHe-1 (A) supercomputer located at National Supercomputer Center in Tianjin, China (http://nscc-tj.gov.cn/en/resources/resources_1.asp#TH-1A). This piece of work was completed in 4 × 24 h of wall time on eight computing nodes with 96 CPU cores and 96 GB RAM. In what follows, we display the modeled results and compare them with the solar coronal and interplanetary observations.

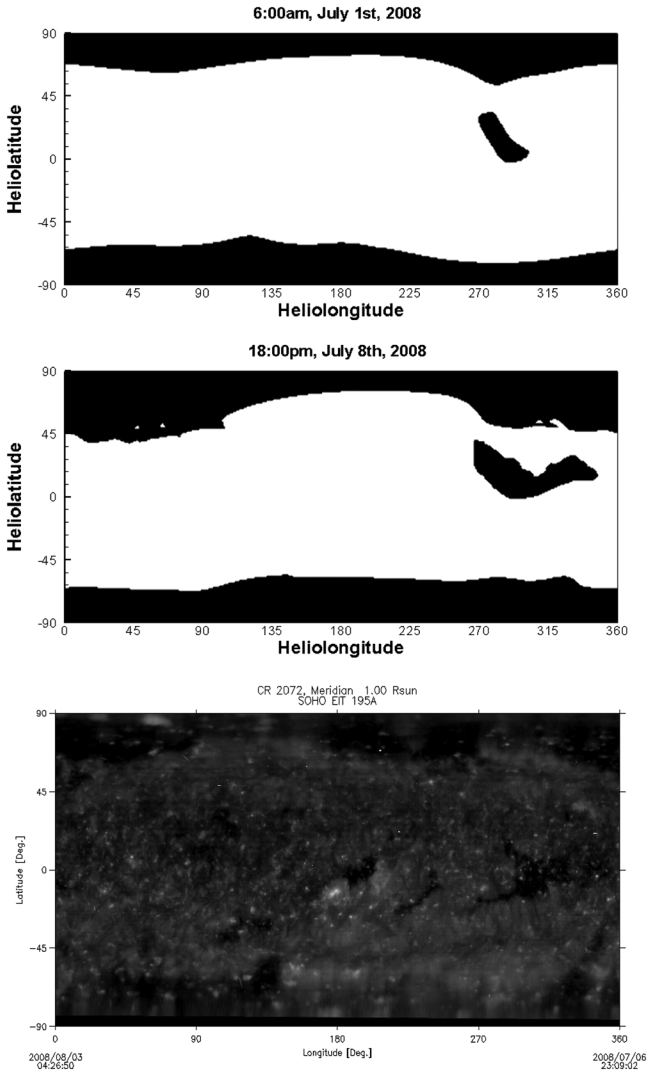

Figure 2. The synoptic maps of the open and closed field distributions obtained from (upper) the steady-state MHD model, (middle) the data-driven MHD model, and (bottom) the EIT observations at 195 Å.

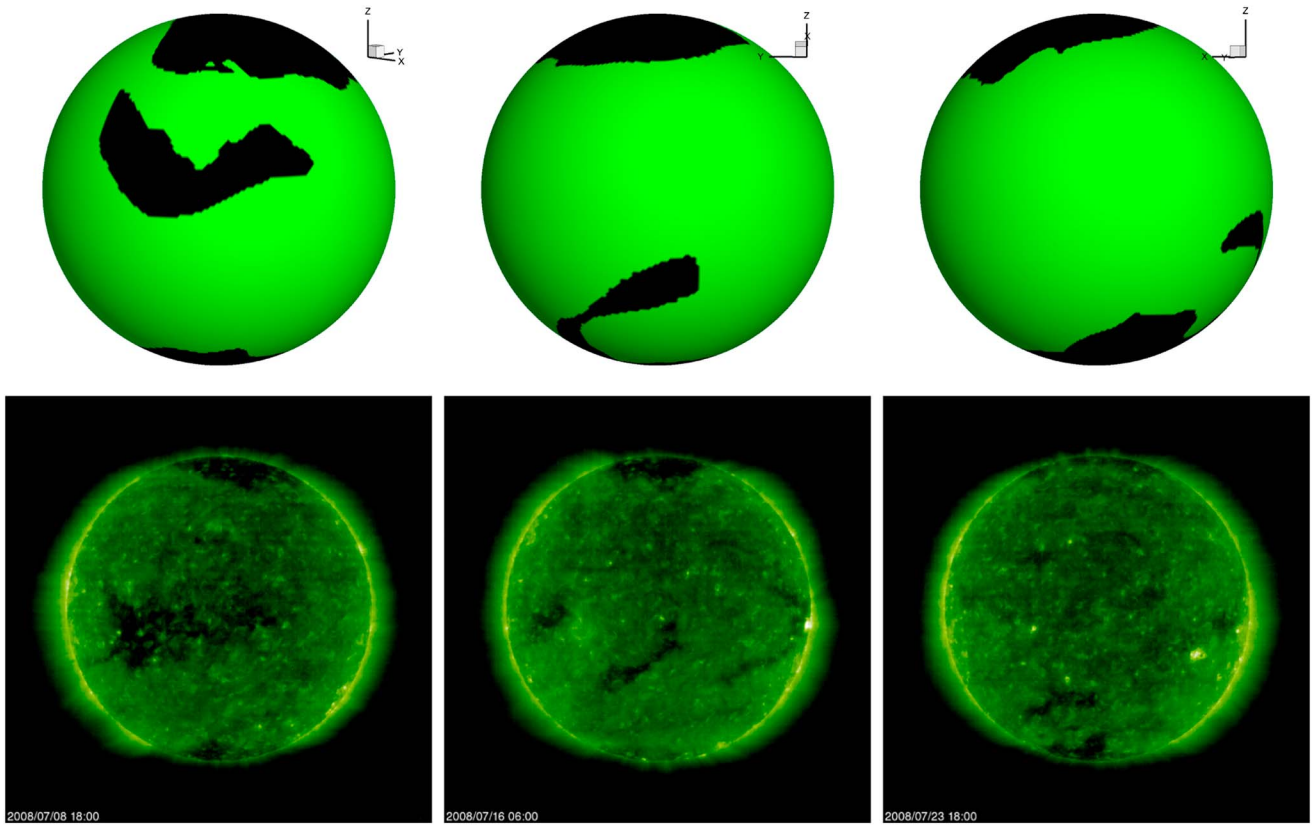

Figure 3. The open and closed field distributions from (top row) the data-driven MHD model results and (bottom row) the EIT observations at 195 Å on 8 July (left column), 16 July (middle column), and 23 July (right column).

Figure 2 displays the synoptic maps of open field distributions at 1 R_s from the initial steady MHD result constrained by the synoptic map on 1 July (the top panel), the solution of the data-driven model result on 8 July (the middle panel), and the SOHO/EIT observations (http://lasco-www.nrl.navy.mil/carr_maps) during CR 2072 which lasted from 6 July to 3 August (the bottom panel). The modeled coronal holes (i.e., the open field regions) are shaded black.

From both the observations and the simulations in Figure 2, we find that the northern polar coronal hole (PCH) occupies the largest area for the data-driven MHD model and the smallest area for the steady-state MHD model. The median latitudes of the northern PCH's equatorward boundary from the data-driven MHD model, the steady-state MHD model, and the EIT observation are 63°, 72°, and 68°. For the southern PCH, the data-driven MHD model and the steady-state MHD model give similar coverage, but the EIT observations cannot accurately record it because the spacecraft orbited 6°north of the solar equator. In addition, both the data-driven MHD model and the steady-state MHD model capture the equatorial coronal hole (ECH) centered around the longitude of 290°, but the size and shape from the former are more close to those from the EIT observations. It should be noted that compared with the EIT observations, the ECH from the data-driven and steady-state models is a little northward. *Abramenko and Yurchyshyn* [2010] investigated this coronal hole and found that it lasted almost 2 years and finally vanished in June 2009. Although the data-driven model captures this ECH with reasonable accuracy, it fails to capture the small-sized ECHs centered on 90°and 190°in longitude.

Figure 3 shows the open field distributions from the data-driven MHD model and the EIT observations at 195 Å on the specified dates. These modeled images show relatively good agreements with the observations except that small-sized dark regions near the solar equator on 16 July are not well reproduced in the simulated image. In addition, the north PCH covers a little larger area in the modeled image on 31 July. It should be noted that some observed dark regions in Figures 2 and 3 may be transient coronal holes associated with coronal mass ejections (CMEs) because there were many CMEs remotely recorded in the STEREO data set available from http://sidc.oma.be/cactus. It should also be noted that CMEs are not the sole cause for the

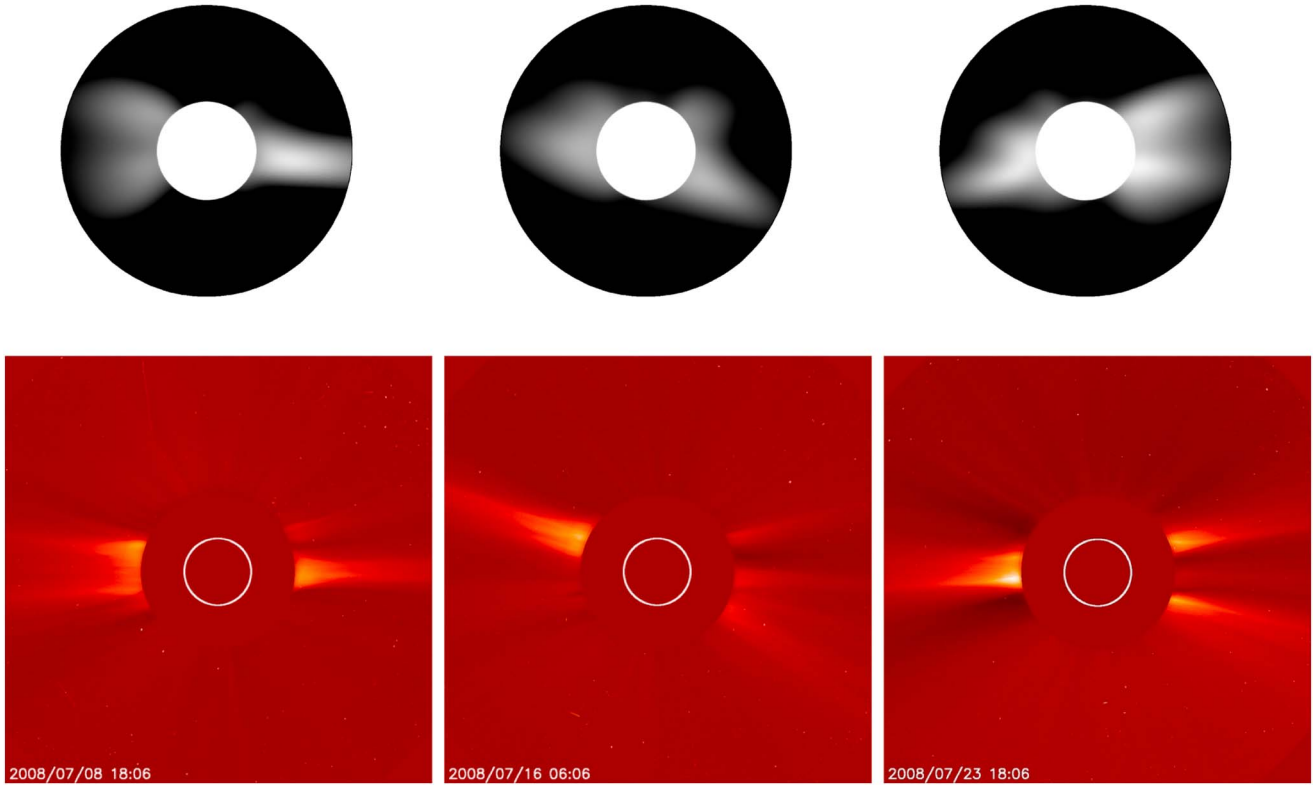

Figure 4. The white-light polarized brightness images from (top row) the data-driven MHD model and (bottom row) from the LASCO/SOHO observations on 8 July (left column), 16 July (middle column), and 23 July (right column).

missing small-sized CHs in the simulated result because some of the effects that occur in the corona are caused by processes that only occur in the corona, such as reconnection or destabilization of structures following magnetic shearing [e.g., *Dunn et al.*, 2005]. In addition, it is probably impossible to map CME transient features in detail. The thorough analyses are beyond the scope of this paper.

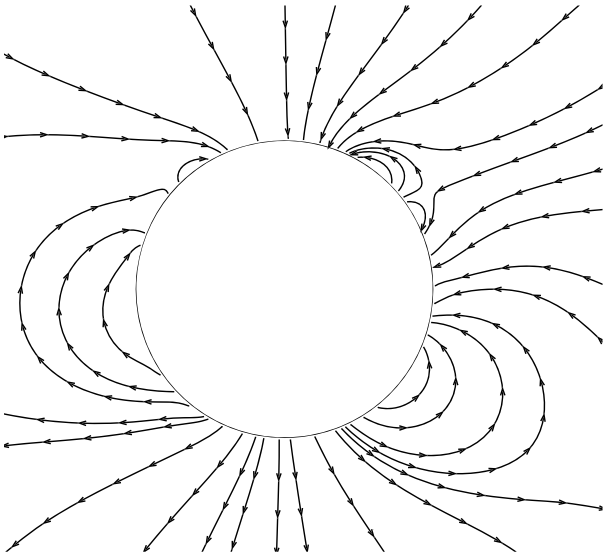

Figure 5. The solar coronal magnetic field lines from the data-driven MHD model on 17 July 2008. The field lines are projected on the meridian plane perpendicular to the Sun-Earth direction; the circle indicates the solar surface.

Figure 4 shows the white-light polarized brightness (pB) images from the data-driven MHD model and from the Large Angle and Spectrometric Coronagraph (LASCO)/SOHO observations on three specified dates. It is well known that the bright regions shown in pB images are indicators of the dense streamers or pseudostreamers viewed on the limbs and the dark regions to the coronal holes [*Blackwell and Petford*, 1966a, 1966b; *Frazin et al.*, 2007].

In Figure 4, the bright streamers span a narrow range of lower latitudes and the dark PCHs dominate higher latitudes. Almost every observed image shows very bright long streamer-like structures at the east and west limbs, although the correspondent bright structures seem wider in the simulation results. In the image on 16 July, we expect the bright configurations at both limbs in the Northern

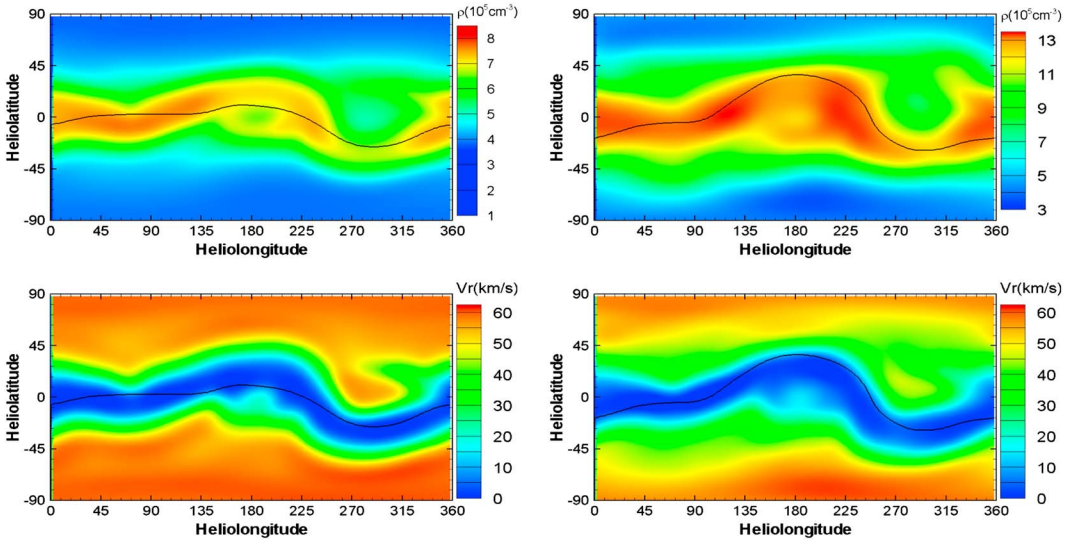

Figure 6. Synoptic maps of the (top row) proton number density and (bottom row) radial bulk speed on 1 July (left column) and 14 July (right column) at 2.5 solar radii. The black lines indicate the locations where $B_r = 0$.

Hemisphere result from the pseudostreamers at Carrington longitudes 110°and 290°[*Rusšin et al.*, 2010]. In order to clearly demonstrate the pseudostreamer structures, we present the magnetic field lines near the Sun projected on the sky plane on 17 July in Figure 5. Additionally, the other two wide bright structures near the solar equator are associated with the abrupt deflect of heliospheric current sheet (HCS) around Carrington longitude 270°, which can be seen clearly in Figure 6.

Figure 6 presents the synoptic maps of the proton number density and radial bulk speed on 1 July and 14 July at 2.5 R_s. Comparing the results from the steady-state MHD model on 1 July and the data-driven MHD model on 14 July, we find that both models achieve roughly similar global distributions of the solar wind parameters. The HCSs are basically coincident with the regions of high density and low speed, while the regions poleward of 45° are covered with the solar wind of high speed and lower density. However, a bulge centered at the longitude of 220° appears in the HCS profile in the data-driven model's result. As a result, the HCS becomes more tilted than that from the steady MHD model's result. A high-density region is also present near $(\theta, \phi) = (-20°, 290°)$ in the data-driven model's result.

In order to further validate our data-driven solar wind model, we plot the loci of the Alfvén surfaces (ASs) in the meridian planes of 270°–90° in Figure 7. The figure demonstrates that the ASs lie between 9 and 12 R_s in the PCHs and between 4 and 15 R_s in the coronal streamers. This is consistent with the recent studies that suggest that the Alfvén surfaces are located at a wide range of possible heliocentric distances, from 6 to 30 R_s.

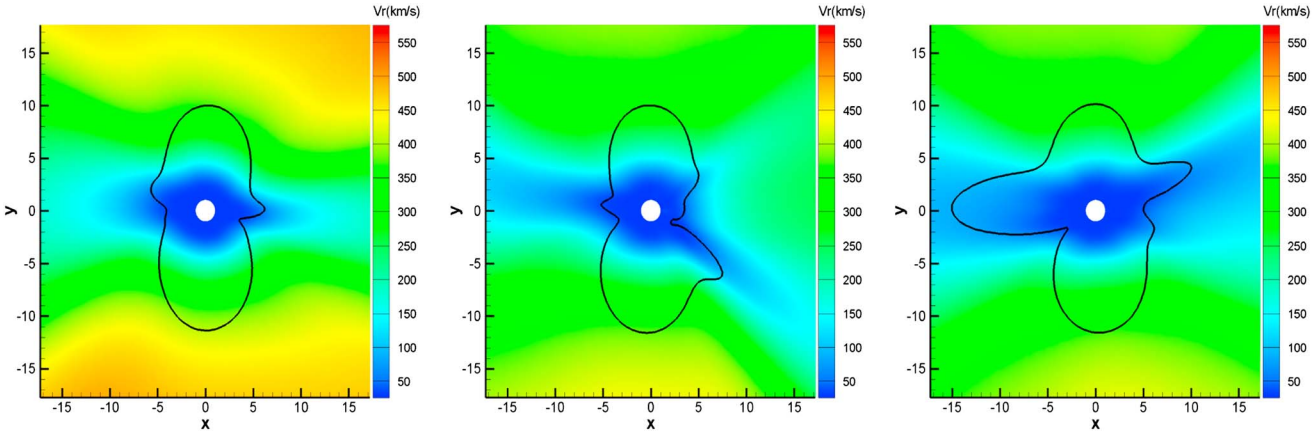

Figure 7. Contours of solar wind radial bulk speeds in the 270°–90° meridian planes on (left) 8 July, (middle) 16 July, and (right) 23 July. The black lines indicate the locations where the Alfvénic Mach number is 1.

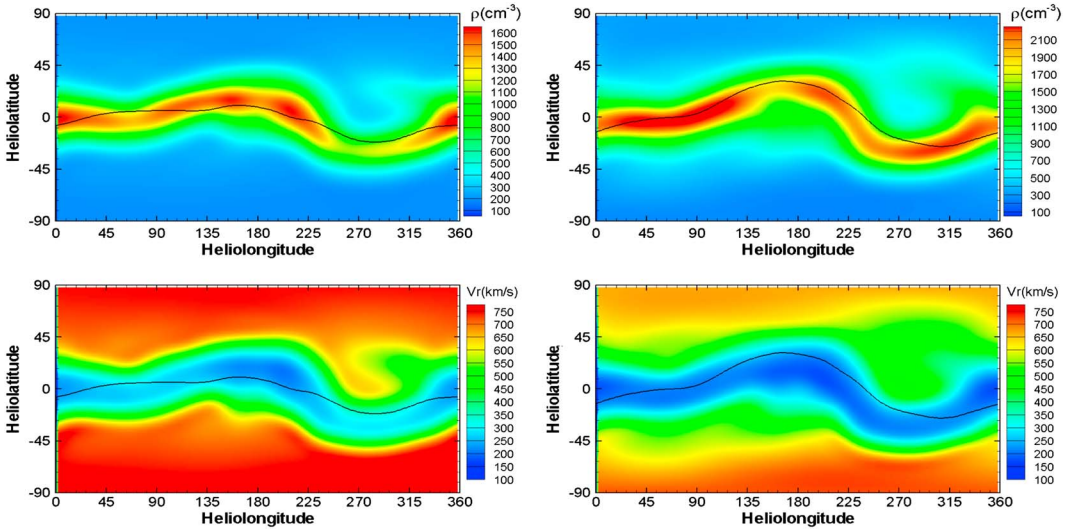

Figure 8. Synoptic maps of the (top row) proton number density and (bottom row) radial bulk speed on 1 July (left column) and 14 July (right column) at 20 solar radii. The black lines indicate the locations where $B_r = 0$.

Zhao and Hoeksema [2010] determined the outer limit of AS in coronal streamers to be 10–14 R_s around solar minimum. *Sheeley et al.* [2004] inferred that the AS in coronal streamers should be outside of 6 R_s. *Goelzer et al.* [2014] employed a model of the interplanetary magnetic field to obtain the location of the AS from sunspot numbers and then placed the AS at 15 R_s during solar minimum and 30 R_s during solar maximum. *DeForest et al.* [2014] identified the AS by analyzing a sequence of coronagraph images from STEREO-A/COR2 and determined the AS's altitude to be beyond 15 R_s in the streamer belt and 12 R_s in the coronal hole.

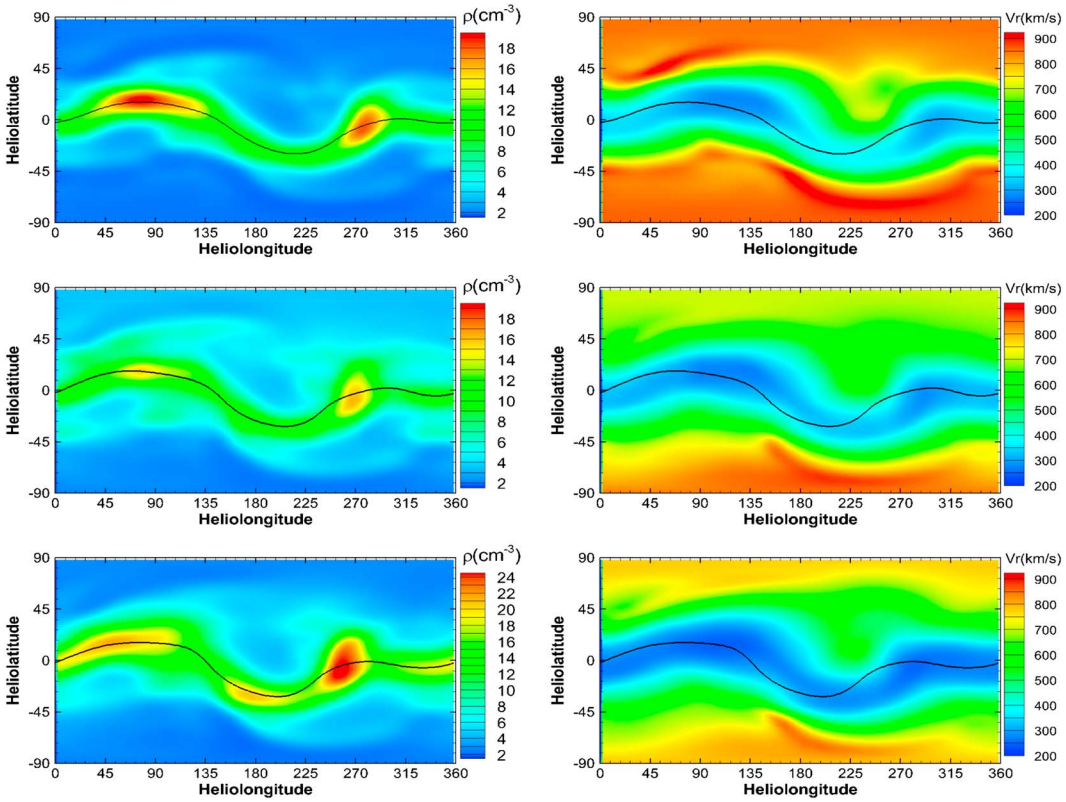

Figure 9. Synoptic maps of the (left column) proton number density and (right column) radial bulk speed on 1 July (top row), 14 July (middle row), and 23 July (bottom row) at 1 AU. The black lines indicate the locations where $B_r = 0$.

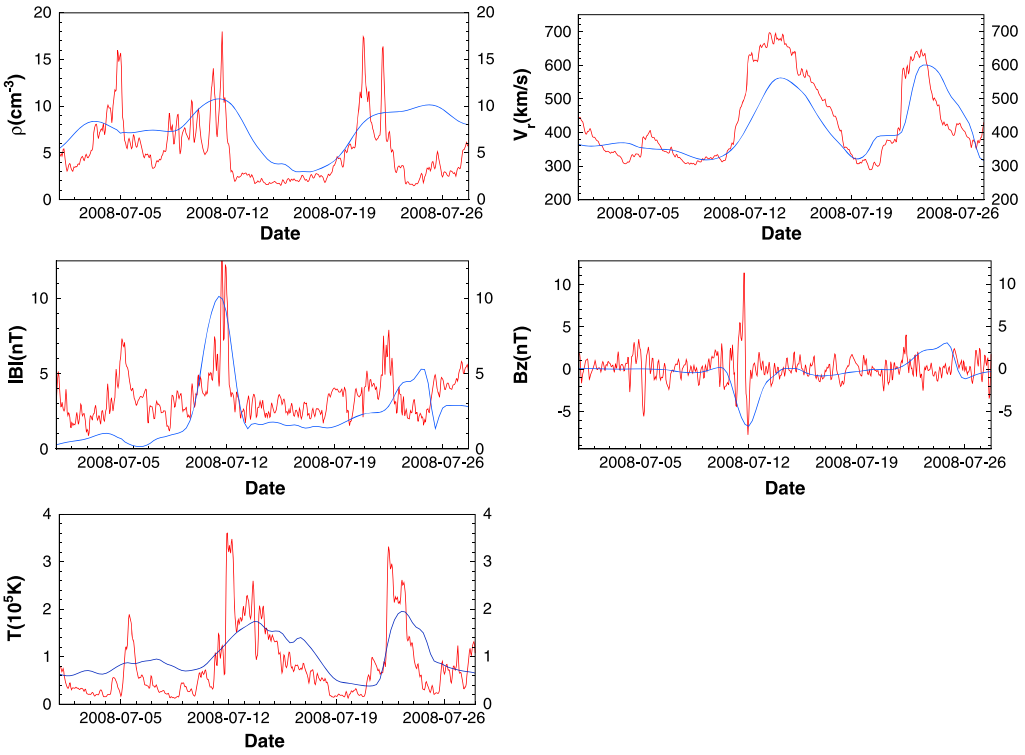

Figure 10. Comparison between simulation results and OMNI data. The red lines are OMNI in situ measurements, and the blue lines represent our simulation results. From top left to bottom right, the parameters are the proton number density, radial bulk speed, total magnetic field strength, and the temperature.

It should be noted that, in the figure, the sunward concaved structures on the ASs result from the minima of the local coronal magnetic field and the Alfvén speed.

Figure 8 exhibits the synoptic maps of the proton number density and radial bulk speed on 1 July (left column) and 14 July (right column) at 20 R_s. Comparing the results on 1 July and 14 July, we can find some perceptible changes of the solar wind between the results from both models, although the main structures are very similar including the basic shape of the heliospheric current sheet (HCS) and the global distributions of the plasma parameters. In this figure, the prominent differences between the results from the steady MHD model and the data-driven MHD model are the appearances of the northward bulge of the HCS around the longitude of 180° and the associated high-dense structure centered at $(\theta, \phi) = (30°, 180°)$ in the data-driven MHD model. Another significant change is the southward shift of the HCS near the longitude of 0°. Figure 9 presents the synoptic maps of the proton number density and radial bulk speed at 1 AU. This figure shows that the high-dense structure centered at $(\theta, \phi)=(30°, 180°)$ at 20 R_s shifts to $(\theta, \phi)=(30°, 90°)$. Comparing with Figure 6, the hump of the HCS becomes wider and flatter and the trough centered at longitude 200°becomes deeper and more apparent.

Figure 10 compares the simulation results from the data-driven MHD model and the OMNI data at 1 AU. The comparison shows that the result of the data-driven model roughly captures the main features of the solar wind observation. In the figure, both the observation and the data-driven model show similar variation trends of the radial bulk speed, total magnetic field strength, and the temperature. Both the measurements and the data-driven model capture two high-speed streams with reasonable accuracy. The simulation obtains relatively higher density and lower solar wind temperature than the OMNI data. The modeled hump of the solar wind speed centered on 14 July is somewhat lower than the observation, but the simulated hump on 23 July fits the OMNI data very well. Indeed, there are some discrepancies between the simulation and the observation. The total magnetic field strength from the simulated result is much lower than that observed for the most part of the investigated period, and the improvement of this situation requires the modelers' dedicated efforts.

5. Concluding Remarks and Discussions

In this article, we propose a data-driven MHD model to achieve the time-varying coronal structure and interplanetary solar wind background and adopt it to investigate the evolution of the solar corona and solar wind from 1 July to 11 August in 2008 using the high-cadence GONG's synoptic maps of photospheric LOS magnetic field. The model is based on the SIP-AMR-CESE MHD model and the bottom boundary conditions specified by using the differential rotation corrected GONG's synoptic maps, the PNC method, and the mass flux limit on the solar photosphere.

The data-driven model reproduces many global coronal features and interplanetary solar wind structures although there are some discrepancies between the modeled results and the observations. The model not only achieves the coronal pattern high latitudinal PCHs of high speed and low density and low-latitudinal streamers of low speed and high density but also reproduces the long-duration ECH around the longitude of 290°but fails to capture the small-sized ECHs centered around 90°and 190°in longitude. Besides, the model captures the pseudostreamers. The modeled heliocentric distances of the AS lie in the range that previous work has presented. The results from the data-driven MHD model roughly obtain the same global distribution of the solar wind parameters as observed near 1 AU. The data-driven model obtains similar trends of the solar wind and reproduces the increases of in situ speed centered on 14 and 23 July, although the simulated maximum speed of the increase for the former one is lower than the observed. However, the total magnetic field strength from the simulated result is lower than the observed during most of the investigated interval. In addition, the simulation obtains higher density and lower solar wind temperature than the OMNI data.

However, what we present here is just a result obtained at solar minimum when the coronal background does not vary significantly. Some improvements are needed for the model to capture the observations of the background solar wind with higher accuracy. First, in order for the observed magnetic field to fit the corona model, we must perform some smoothing procedures for the observed data. The model presented here fails to reproduce the small-sized ECHs perhaps due to the over-smoothing of the photospheric magnetic field. Therefore, more suitable smoothing methods should be developed that may reproduce more of these more rapidly varying transient structures. Another solution to the problem may be to couple the solar corona model to the models of lower solar atmosphere that provide these rapid changes in coronal fields and other plasma parameters [e.g., *Lionello et al.*, 2001; *Gudiksen and Nordlund*, 2005; *Peter*, 2007; *Bingert and Peter*, 2011; *Amari et al.*, 2013; *van Driel-Gesztelyi et al.*, 2014; *Titov et al.*, 2014; *Jiang et al.*, 2013, 2014]. In addition, the incorporation of the corona densities and plasma velocities derived from IPS data into the specification of the bottom boundary conditions can also enhance the ability of our model to better capture rapidly changing interplanetary solar wind structures associated with transient events such as CMEs. Second, we adopt the 6 h cadence synoptic maps to drive our model without special selection in this paper. In fact, some maps may contain much noise due to the occurrences of explosive events or some unknown reasons. We should develop some proper criteria to select the data in order for us to maintain the stability of the computation and achieve more realistic solar background. Other considerations include utilizing higher-resolution data from solar dynamics observatory [*Henney et al.*, 2009; *Scherrer et al.*, 2012; *Liu et al.*, 2012] and full disk vector magnetograms in our data-driven model. It should be noted that although the preliminary study from a very small 4 week selection of data during solar minimum provides the same mechanism for the rest of time, other effective measures will be needed to deal with far greater problems encountered when the model is used in the periods of high solar activity, during which the corona becomes very active, or CMEs dominate the corona and in situ record. We expect that the data-driven MHD model after further improvements can provide a numerical tool for investigating solar explosive phenomena and their associated interplanetary evolution process.

Acknowledgments

The work was jointly supported by by the National Basic Research Program of China (grant 2012CB825601), the National Natural Science Foundation of China (grants 41231068, 41274192, 41531073, 41574171, and 41374176), the Knowledge Innovation Program of the Chinese Academy of Sciences (grant KZZD-EW-01-4), and the Specialized Research Fund for State Key Laboratories. This work utilizes data obtained by the Global Oscillation Network Group (GONG) program, managed by the National Solar Observatory, which is operated by AURA, Inc. under a cooperative agreement with the National Science Foundation. The data were acquired by instruments operated by the Big Bear Solar Observatory, High Altitude Observatory, Learmonth Solar Observatory, Udaipur Solar Observatory, Instituto de Astrofísica de Canarias, and Cerro Tololo Interamerican Observatory. The SOHO/LASCO data used here are produced by a consortium of the Naval Research Laboratory (USA), Max-Planck-Institut fuer Aeronomie (Germany), Laboratoire d'Astronomie (France), and the University of Birmingham (UK). SOHO is a project of international cooperation between ESA and NASA. The OMNI data are obtained from the GSFC/SPDF OMNIWeb interface at http://omniweb.gsfc.nasa.gov. The work was carried out at National Supercomputer Center in Tianjin, China and the calculations were performed on TianHe-1 (A).

References

Abramenko, V., and V. Yurchyshyn (2010), Intermittency and multifractality spectra of the magnetic field in solar active regions, *Astrophys. J.*, *722*, 122–130.

Amari, T., J.-J. Aly, A. Canou, and Z. Mikic (2013), Reconstruction of the solar coronal magnetic field in spherical geometry, *Astron. Astrophys.*, *553*, A43, doi:10.1051/0004-6361/201220787.

Arge, C. N., and V. J. Pizzo (2000), Improvement in the prediction of solar wind conditions using near-real time solar magnetic field updates, *J. Geophys. Res.*, *105*(A5), 10,465–10,479.

Arge, C. N., E. Hildner, V. J. Pizzo, and J. W. Harvey (2002), Two solar cycles of nonincreasing magnetic flux, *J. Geophys. Res.*, *107*(A10), 1319, doi:10.1029/2001JA000503.

Arge, C. N., D. Odstrcil, V. J. Pizzo, and L. R. Mayer (2003), Improved method for specifying solar wind speed near the Sun, in *Solar Wind Ten, American Institute of Physics Conference Series*, vol. 679, edited by M. Velli et al., pp. 190–193, AIP, Melville, New York.

Arge, C. N., J. G. Luhmann, D. Odstrcil, C. J. Schrijver, and Y. Li (2004), Stream structure and coronal sources of the solar wind during the May 12th, 1997 CME, *J. Atmos. Sol. Terr. Phys.*, *66*, 1295–1309.
Arge, C. N., C. J. Henney, I. G. Hernandez, W. A. Toussaint, J. Koller, and H. C. Godinez (2013), Modeling the corona and solar wind using ADAPT maps that include far-side observations, *AIP Conf. Proc.*, *1539*(1), 11–14.
Aschwanden, M. J., et al. (2008), Theoretical modeling for the STEREO mission, *Space Sci. Rev.*, *136*, 565–604.
Balsara, D. S., and D. Spicer (1999), Maintaining pressure positivity in magnetohydrodynamic simulations, *J. Comput. Phys.*, *148*, 133–148.
Bingert, S., and H. Peter (2011), Intermittent heating in the solar corona employing a 3D MHD model, *Astron. Astrophys.*, *530*, A112, doi:10.1051/0004-6361/201016019.
Blackwell, D. E., and A. D. Petford (1966a), Observations of the 1963 July 20 solar eclipse: I. Spectroscopic separation of the F and K components of the solar corona at large distances from the Sun, *Mon. Not. R. Astron. Soc.*, *131*, 383–398.
Blackwell, D. E., and A. D. Petford (1966b), Observations of the 1963 July 20 solar eclipse: II. The electron density in the solar corona in the region $5 < R/R_0 < 16$ obtained from measurements of Fraunhofer line depth and the polarization of the F corona, *Mon. Not. R. Astron. Soc.*, *131*, 399–406.
Burlaga, L. F., N. F. Ness, Y.-M. Wang, and N. R. Sheeley (2002), Heliospheric magnetic field strength and polarity from 1 to 81 AU during the ascending phase of solar cycle 23, *J. Geophys. Res.*, *107*(A11), 1410, doi:10.1029/2001JA009217.
Cohen, O., I. V. Sokolov, I. I. Roussev, and T. I. Gombosi (2008), Validation of a synoptic solar wind model, *J. Geophys. Res.*, *113*, A03104, doi:10.1029/2007JA012797.
DeForest, C. E., H. T. A., and M. D. J. (2014), Inbound waves in the solar corona: A direct indicator of Alfvén surface location, *Astrophys. J.*, *787*, 124, doi:10.1088/0004-637X/787/2/124.
Dryer, M. (2007), Space weather simulation in 3D MHD from the Sun to the Earth and beyond to 100 AU: A modeler's perspective of the present state of the art, *Asian J. Phys.*, *16*, 97.
Dunn, T., B. V. Jackson, P. P. Hick, A. Buffington, and X. P. Zhao (2005), Comparative analyses of the CSSS calculation in the UCSD tomographic solar observations, *Sol. Phys.*, *227*, 339–353.
Feng, X. S., Y. F. Zhou, and S. T. Wu (2007), A novel numerical implementation for solar wind modeling by the modified conservation element/solution element method, *Astrophys. J.*, *655*(2), 1110–1126.
Feng, X. S., L. P. Yang, C. Q. Xiang, S. T. Wu, Y. F. Zhou, and D. K. Zhong (2010), Three-dimensional solar wind modeling from the Sun to Earth by a SIP-CESE MHD model with a six-component grid, *Astrophys. J.*, *723*(1), 300–319.
Feng, X. S., C. Q. Xiang, and D. K. Zhong (2011a), The state-of-art of three-dimensional numerical study for corona-interplanetary process of solar storms (in Chinese), *Sci. Sin. Terrae*, *41*, 1–28.
Feng, X. S., S. H. Zhang, C. Q. Xiang, L. P. Yang, C. W. Jiang, and S. T. Wu (2011b), A hybrid solar wind model of the CESE+HLL method with a Yin-Yang overset grid and an AMR grid, *Astrophys. J.*, *734*, 50.
Feng, X. S., C. W. Jiang, C. Q. Xiang, X. P. Zhao, and S. T. Wu (2012a), A data-driven model for the global coronal evolution, *Astrophys. J.*, *758*(1), 62.
Feng, X. S., L. P. Yang, C. Q. Xiang, Y. Liu, X. P. Zhao, and S. T. Wu (2012b), Numerical study of the global corona for CR 2055 driven by daily-updated synoptic magnetic field, in *Proceedings of a 6th Internation Conference Held at Velancia, Spain June 13-17, 2011*, vol. 459, edited by N. V. Pogorelov et al., p. 202, Astron. Soc. of the Pacific Conf. Ser., San Francisco, Calif.
Feng, X. S., L. P. Yang, C. Q. Xiang, Y. Liu, X. P. Zhao, and S. T. Wu (2012c), Numerical study of the global corona for CR 2055 driven by daily-updated synoptic magnetic field, in *Numerical Modeling of Space Plasma Slows (ASTRONUM 2011)*, vol. 459, pp. 202–208, Astron. Soc. of the Pacific Conf. Ser., San Francisco, Calif.
Feng, X. S., C. Q. Xiang, and D. K. Zhong (2013), Numerical study of interplanetary solar storms (in Chinese), *Sci. Sin. Terrae*, *43*, 912.
Feng, X. S., C. Q. Xiang, D. K. Zhong, Y. F. Zhou, L. P. Yang, and X. P. Ma (2014a), SIP-CESE MHD model of solar wind with adaptive mesh refinement of hexahedral meshes, *Comput. Phys. Commun.*, *185*(7), 1965–1980.
Feng, X. S., M. Zhang, and Y. F. Zhou (2014b), A new three-dimensional solar wind model in spherical coordinates with a six-component grid, *Astrophys. J. Suppl. Ser.*, *723*, 300–319.
Frazin, R. A., A. M. Vásquez, F. Kamalabadi, and H. Park (2007), Three-dimensional tomographic analysis of a high-cadence LASCO-C2 polarized brightness sequence, *Astrophys. J. Lett.*, *671*, L201–L204.
Goelzer, M. L., C. W. Smith, N. A. Schwadron, and K. G. McCracken (2013), An analysis of heliospheric magnetic field flux based on sunspot number from 1749 to today and prediction for the coming solar minimum, *J. Geophys. Res. Space Physics*, *118*, 7525–7531, doi:10.1002/2013JA019404.
Goelzer, M. L., N. A. Schwadron, and C. W. Smith (2014), An analysis of Alfvén radius based on sunspot number from 1749 to today, *J. Geophys. Res. Space Physics*, *119*, 115–120, doi:10.1002/2013JA019420.
Gombosi, T., D. L. De Zeeuw, K. G. Powell, A. J. Ridley, I. V. Sokolov, Q. F. Stout, and G. Tóth (2003), Adaptive mesh refinement for global magnetohydrodynamic simulation, in *Space Plasma Simulation, Lecture Notes in Physics*, vol. 615, edited by J. Büchner, M. Scholer, and C. Dum, Springer, Berlin Heidelberg.
Gonzalez, W. D., B. T. Tsurutani, A. L. C. Gonzalez, E. J. Smith, F. Tang, and S.-I. Akasofu (1989), Solar wind-magnetosphere coupling during intense magnetic storms (1978-1979), *J. Geophys. Res.*, *94*(A7), 8835–8851.
Gudiksen, B. V., and Å. Nordlund (2005), An ab initio approach to the solar coronal heating problem, *Astrophys. J.*, *618*, 1020–1030.
Harvey, J. W., et al. (1996), The global oscillation network group (GONG) project, *Science*, *272*, 1284–1286.
Hayashi, K. (2005), Magnetohydrodynamic simulations of the solar corona and solar wind using a boundary treatment to limit solar wind mass flux, *Astrophys. J. Suppl. Ser.*, *161*, 480–494.
Hayashi, K. (2012), An MHD simulation model of time-dependent co-rotating solar wind, *J. Geophys. Res.*, *117*, A08105, doi:10.1029/2011JA017490.
Hayashi, K. (2013), An MHD simulation model of time-dependent global solar corona with temporally varying solar-surface magnetic field maps, *J. Geophys. Res. Space Physics*, *118*, 6889–6906, doi:10.1002/2013JA018991.
Hayashi, K., X. P. Zhao, and Y. Liu (2008), MHD simulations of the global solar corona around the Halloween event in 2003 using the synchronic frame format of the solar photospheric magnetic field, *J. Geophys. Res.*, *113*, A07104, doi:10.1029/2007JA012814.
Henney, C. J., C. U. Keller, J. W. Harvey, M. K. Georgoulis, N. L. Hadder, A. A. Norton, N.-E. Raouafi, and R. M. Toussaint (2009), SOLIS vector spectromagnetograph: Status and science, in *Solar Polarization 5: In Honor of Jan Stenflo*, vol. 405, edited by S. V. Berdyugina, K. N. Nagendra, and R. Ramelli, p. 47, ASP, San Francisco, Calif.
Hernández, I. G., F. Hill, and C. Lindsey (2007), Calibration of seismic signatures of active regions on the far side of the Sun, *Astrophys. J.*, *669*(2), 1382–1389.
Hickmann, K. S., H. C. Godinez, C. J. Henney, and C. N. Arge (2015), Data assimilation in the ADAPT Photospheric Flux Transport model, *Sol. Phys.*, *290*(4), 1105–1118.

Hill, F., G. Fischer, J. Grier, J. W. Leibacher, H. B. Jones, P. P. Jones, R. Kupke, and R. T. Stebbins (1994a), The global oscillation network group site survey, 1: Data collection and analysis methods, *Sol. Phys.*, *152*, 321–349.
Hill, F., et al. (1994b), The global oscillation network group site survey, 2: Results, *Sol. Phys.*, *152*, 351–379.
Intriligator, D. S., T. Detman, G. Gloecker, C. Gloeckler, M. Dryer, W. Sun, J. Intriligator, and C. Deehr (2012), Pickup protons: Comparisons using the three-dimensional MHD HHMS-PI model and Ulysses SWICS measurements, *J. Geophys. Res.*, *117*, A06104, doi:10.1029/2011JA017424.
Jackson, B. V., P. P. Hick, A. Buffington, M. M. Bisi, J. M. Clover, M. Tokumaru, M. Kojima, and K. Fujiki (2011), Three-dimensional reconstruction of heliospheric structure using iterative tomography: A review, *J. Atmos. Sol. Terr. Phys.*, *73*, 1214–1227.
Jackson, B. V., et al. (2015), The UCSD kinematic IPS solar wind boundary and its use in the ENLIL 3-D MHD prediction model, *Space Weather*, *13*, 104–115, doi:10.1002/2014SW001130.
Janhunen, P., M. Palmroth, T. Laitinen, I. Honkonen, L. Juusola, G. Facskó, and T. Pulkkinen (2012), The GUMICS-4 global MHD magnetosphere-ionosphere coupling simulation, *J. Atmos. Sol. Terr. Phys.*, *80*, 48–59.
Jian, L. K., P. J. MacNeice, A. Taktakishvili, D. Odstrcil, B. V. Jackson, H.-S. Yu, P. Riley, I. V. Sokolov, and R. M. Evans (2015), Validation for solar wind prediction at Earth: Comparison of coronal and heliospheric models installed at the CCMC, *Space Weather*, *13*, 316–338, doi:10.1002/2015SW001174.
Jiang, C. W., X. S. Feng, S. T. Wu, and Q. Hu (2013), Magnetohydrodynamic simulation of a sigmoid eruption of active region 11283, *Astrophys. J. Lett.*, *771*(2), L30.
Jiang, C. W., S. T. Wu, X. S. Feng, and Q. Hu (2014), Formation and eruption of an active region sigmoid. I. A study by nonlinear force-free field modeling, *Astrophys. J.*, *780*(1), 55, doi:10.1088/0004-637X/780/1/55.
Lax, P., and B. Wendroff (1960), Systems of conservation laws, *Commun. Pure Appl. Math.*, *13*(2), 217–237.
Lionello, R., J. A. Linker, and Z. Mikić (2001), Including the transition region in models of the large-scale solar corona, *Astrophys. J.*, *546*, 542–551.
Lionello, R., P. Riley, J. A. Linker, and Z. Mikić (2005), The effects of differential rotation on the magnetic structure of the solar corona: Magnetohydrodynamic simulations, *Astrophys. J.*, *625*(1), 463–473.
Lionello, R., C. Downs, J. A. Linker, T. Török, P. Riley, and Z. Mikić (2013), Magnetohydrodynamic simulations of interplanetary coronal mass ejections, *Astrophys. J.*, *777*(1), 76, doi:10.1088/0004-637X/777/1/76.
Liu, Y., J. T. Hoeksema, X. Zhao, and R. M. Larson (2007), MDI synoptic charts of magnetic field: Interpolation of polar fields, in *American Astronomical Society Meeting Abstracts #210, Bulletin of the American Astronomical Society*, vol. 39, p. 129, Am. Astron. Soc., Washington, D. C.
Liu, Y., et al. (2012), Comparison of line-of-sight magnetograms taken by the solar dynamics observatory/helioseismic and magnetic imager and solar and heliospheric observatory/Michelson doppler imager, *Sol. Phys.*, *279*(1), 295–316.
Lugaz, N., C. Downs, K. Shibata, I. I. Roussev, A. Asai, and T. I. Gombosi (2011), Numerical investigation of a coronal mass ejection from an anemone active region: Reconnection and deflection of the 2005 August 22 eruption, *Astrophys. J.*, *738*, 127, doi:10.1088/0004-637X/738/2/127.
Mackay, D. H., and A. A. van Ballegooijen (2006), Models of the large-scale corona. I. Formation, evolution, and liftoff of magnetic flux ropes, *Astrophys. J.*, *641*(1), 577–589.
MacNeice, P., K. M. Olson, C. Mobarry, R. de Fainchtein, and C. Packer (2000), PARAMESH: A parallel adaptive mesh refinement community toolkit, *Comput. Phys. Commun.*, *126*(3), 330–354.
Manchester, W. B. I., A. Vourlidas, G. Tóth, N. Lugaz, I. I. Roussev, I. V. Sokolov, T. I. Gombosi, D. L. De Zeeuw, and M. Opher (2008), Three-dimensional MHD simulation of the 2003 October 28 coronal mass ejection: Comparison with LASCO coronagraph observations, *Astrophys. J.*, *684*, 1448–1460.
McComas, D. J., R. W. Ebert, H. A. Elliott, B. E. Goldstein, J. T. Gosling, N. A. Schwadron, and R. M. Skoug (2008), Weaker solar wind from the polar coronal holes and the whole Sun, *Geophys. Res. Lett.*, *35*, L18103, doi:10.1029/2008GL034896.
Mikić, Z., J. A. Linker, D. D. Schnack, R. Lionello, and A. Tarditi (1999), Magnetohydrodynamic modeling of the global solar corona, *Phys. Plasmas*, *6*(5), 2217–2224.
Nakagawa, Y. (1980), Evolution of solar magnetic fields–A new approach to MHD initial-boundary value problems by the method of nearcharacteristics, *Astrophys. J.*, *240*, 275–299.
Nakagawa, Y. (1981a), Evolution of magnetic field and atmospheric response. I - Three-dimensional formulation by the method of projected characteristics, *Astrophys. J.*, *247*, 707–733.
Nakagawa, Y. (1981b), Evolution of magnetic field and atmospheric responses. II - Formulation of proper boundary equations, *Astrophys. J.*, *247*, 719–733.
Nakagawa, Y., Y. Q. Hu, and S. T. Wu (1987), The method of projected characteristics for the evolution of magnetic arches, *Astron. Astrophys.*, *179*, 354–370.
Nakamizo, A., T. Tanaka, Y. Kubo, S. Kamei, H. Shimazu, and H. Shinagawa (2009), Development of the 3-D MHD model of the solar corona-solar wind combining system, *J. Geophys. Res.*, *114*, A07109, doi:10.1029/2008JA013844.
Neugebauer, M., et al. (1998), Spatial structure of the solar wind and comparisons with solar data and models, *J. Geophys. Res.*, *103*(A7), 14,587–14,599.
Owens, M. J., C. N. Arge, H. E. Spence, and A. Pembroke (2005), An event-based approach to validating solar wind speed predictions: High-speed enhancements in the Wang-Sheeley-Arge model, *J. Geophys. Res.*, *110*, A12105, doi:10.1029/2005JA011343.
Peter, H. (2007), Modeling the (upper) solar atmosphere including the magnetic field, *Adv. Space Res.*, *39*, 1814–1825.
Powell, K. G., P. L. Roe, T. J. Linde, T. I. Gombosi, and D. L. De Zeeuw (1999), A solution-adaptive upwind scheme for ideal magnetohydrodynamics, *J. Comput. Phys.*, *154*, 284–309.
Riley, P., R. Lionello, J. Linker, Z. Mikić, J. Luhmann, and J. Wijaya (2011), Global MHD modeling of the solar corona and inner heliosphere for the whole heliosphere interval, *Sol. Phys.*, *274*(1–2), 361–377.
Roussev, I. I., T. I. Gombosi, I. V. Sokolov, M. Velli, W. M. IV, D. L. DeZeeuw, P. Liewer, G. Tóth, and J. Luhmann (2003), A three-dimensional model of the solar wind incorporating solar magnetogram observations, *Astrophys. J. Lett.*, *595*(1), L57–L61.
Russin, V., et al. (2010), Comparing eclipse observations of the 2008 August 1 solar corona with an MHD model prediction, *Astron. Astrophys.*, *513*, A45, doi:10.1051/0004-6361/200912778.
Scherrer, P. H., et al. (2012), The helioseismic and magnetic imager (HMI) investigation for the solar dynamics observatory (SDO), *Sol. Phys.*, *275*, 207–227.
Schrijver, C. J., M. L. DeRosa, and A. M. Title (2002), What is missing from our understanding of long-term solar and heliospheric activity?, *Astrophys. J.*, *577*(2), 1006–1012.
Sheeley, N. R., Jr., H. P. Warren, and Y.-M. Wang (2004), The origin of postflare loops, *Astrophys. J.*, *616*, 1224–1231.

Smith, E. J., A. Balogh, R. J. Forsyth, and D. J. McComas (2001), Ulysses in the south polar cap at solar maximum: Heliospheric magnetic field, *Geophys. Res. Lett.*, *28*(22), 4159–4162.
Snodgrass, H. B. (1983), Magnetic rotation of the solar photosphere, *Astrophys. J.*, *270*, 288–299.
Sun, X., Y. Liu, J. Hoeksema, K. Hayashi, and X. Zhao (2011), A new method for polar field interpolation, *Sol. Phys.*, *270*, 9–22.
Svalgaard, L., T. L. Duvall Jr., and P. H. Scherrer (1978), The strength of the Sun's polar fields, *Sol. Phys.*, *58*, 225–239.
Tanaka, T. (1994), Finite volume TVD scheme on an unstructured grid system for three-dimensional MHD simulation of inhomogeneous systems including strong background potential fields, *J. Comput. Phys.*, *111*(2), 381–389.
Titov, V. S., T. Török, Z. Mikic, and J. A. Linker (2014), A method for embedding circular force-free flux ropes in potential magnetic fields, *Astrophys. J.*, *790*, 163, doi:10.1088/0004-637X/790/2/163.
Tóth, G., D. L. D. Zeeuw, T. I. Gombosi, and K. G. Powell (2006), A parallel explicit/implicit time stepping scheme on block-adaptive grids, *J. Comput. Phys.*, *217*(2), 722–758.
Tóth, G., D. L. de Zeeuw, T. I. Gombosi, W. B. Manchester, A. J. Ridley, I. V. Sokolov, and I. I. Roussev (2007), Sun-to-thermosphere simulation of the 28-30 October 2003 storm with the Space Weather Modeling Framework, *Space Weather*, *5*, S06003, doi:10.1029/2006SW000272.
Tóth, G., et al. (2012), Adaptive numerical algorithms in space weather modeling, *J. Comput. Phys.*, *231*(3), 870–903.
Tsurutani, B. T., et al. (2006), Corotating solar wind streams and recurrent geomagnetic activity: A review, *J. Geophys. Res.*, *111*, A07S01, doi:10.1029/2005JA011273.
Tu, C.-Y., and E. Marsch (1995), MHD structures, waves and turbulence in the solar wind: Observations and theories, *Space Sci. Rev.*, *73*, 1–210.
Ulrich, R. K. (1992), Analysis of magnetic fluxtubes on the solar surface from observations at Mt. Wilson of A5250; A5233, in *Cool Stars, Stellar Systems, and the Sun, Astronomical Society of the Pacific Conference Series*, vol. 26, edited by M. S. Giampapa and J. A. Bookbinder, p. 265, Am. Astron. Soc., Washington, D. C.
Ulrich, R. K., S. Evans, J. E. Boyden, and L. Webster (2002), Mount Wilson synoptic magnetic fields: Improved instrumentation, calibration, and analysis applied to the 2000 July 14 flare and to the evolution of the dipole field, *Astrophys. J. Suppl. Ser.*, *139*(1), 259–279.
Usmanov, A. V., and M. L. Goldstein (2006), A three-dimensional MHD solar wind model with pickup protons, *J. Geophys. Res.*, *111*, A07101, doi:10.1029/2005JA011533.
Usmanov, A. V., M. L. Goldstein, B. P. Besser, and J. M. Fritzer (2000), A global MHD solar wind model with WKB Alfvén waves: Comparison with Ulysses data, *J. Geophys. Res.*, *105*(A6), 12,675–12,695.
van der Holst, B., S. Poedts, E. Chané, C. Jacobs, G. Dubey, and D. Kimpe (2005), Modelling of solar wind, CME initiation and CME propagation, *Space Sci. Rev.*, *121*, 91–104.
van der Holst, B., W. B. M. IV, R. A. Frazin, A. M. Vásquez, G. Tóth, and T. I. Gombosi (2010), A data-driven, two-temperature solar wind model with Alfvén waves, *Astrophys. J.*, *725*(1), 1373.
van Driel-Gesztelyi, L., et al. (2014), Coronal magnetic reconnection driven by CME expansion–The 2011 June 7 event, *Astrophys. J.*, *788*(1), 85, doi:10.1088/0004-637X/788/1/85.
Wang, A. H., S. T. Wu, E. Tandberg-Hanssen, and F. Hill (2011), Utilization of multiple measurements for global three-dimensional magnetohydrodynamic simulations, *Astrophys. J.*, *732*, 19, doi:10.1088/0004-637X/732/1/19.
Wang, S., Y. Q. Hu, and S. T. Wu (1982), Full-implicit continuous Eulerian scheme in the spherical coordinates and its applications to solar phenomena, *Sci. Sin. Ser. Math. Phys. Tech. Sci.*, *25*, 1305–1318.
Wang, Y. M., and N. R. Sheeley (1992), On potential-field models of the solar corona, *Astrophys. J.*, *392*, 310–319.
Wang, Y. M., A. G. Nash, and N. R. Sheeley Jr (1989), Magnetic flux transport on the Sun, *Science*, *245*(4919), 712–718.
Wang, Y.-M., J. N. R. Sheeley, J. L. Phillips, and B. E. Goldstein (1997), Solar wind stream interactions and the wind speed-expansion factor relationship, *Astrophys. J. Lett.*, *488*(1), L51–L54.
Wang, Y.-M., J. N. R. Sheeley, and J. Lean (2002), Meridional flow and the solar cycle variation of the Sun's open magnetic flux, *Astrophys. J.*, *580*(2), 1188–1196.
Watermann, J., et al. (2009), Models of solar wind structures and their interaction with the Earth's space environment, *Space Sci. Rev.*, *147*, 233–270.
Wu, C.-C., C. D. Fry, S. T. Wu, M. Dryer, and K. Liou (2007), Three-dimensional global simulation of interplanetary coronal mass ejection propagation from the Sun to the heliosphere: Solar event of 12 May 1997, *J. Geophys. Res.*, *112*, A09104, doi:10.1029/2006JA012211.
Wu, S. T., and M. Dryer (2015), Comparative analyses of current three-dimensional numerical solar wind models, *Sci. China Earth Sci.*, *58*(6), 839–858.
Wu, S. T., W. P. Guo, D. J. Michels, and L. F. Burlaga (1999), MHD description of the dynamical relationships between a flux rope, streamer, coronal mass ejection, and magnetic cloud: An analysis of the January 1997 Sun-Earth connection event, *J. Geophys. Res.*, *104*, 14,789–14,802.
Wu, S. T., A. H. Wang, Y. Liu, and J. T. Hoeksema (2006), Data-driven magnetohydrodynamic model for active region evolution, *Astrophys. J.*, *652*, 800–811.
Xie, H., L. Ofman, and G. Lawrence (2004), Cone model for halo CMEs: Application to space weather forecasting, *J. Geophys. Res.*, *109*, A03109, doi:10.1029/2003JA010226.
Yang, L. P., X. S. Feng, C. Q. Xiang, Y. Liu, X. Zhao, and S. T. Wu (2012), Time-dependent MHD modeling of the global solar corona for year 2007: Driven by daily-updated magnetic field synoptic data, *J. Geophys. Res.*, *117*, A08110, doi:10.1029/2011JA017494.
Yeates, A. R., D. H. Mackay, and A. A. van Ballegooijen (2007), Modelling the global solar corona: Filament chirality observations and surface simulations, *Sol. Phys.*, *245*, 87–107.
Yu, H., B. V. Jackson, P. P. Hick, A. Buffington, N. T. Luckett, D. Odstrcil, C. Wu, and M. Tokumaru (2015), 3D reconstruction of Interplanetary Scintillation (IPS) remote-sensing data: Global solar wind boundaries for driving 3D-MHD models, *Sol. Phys.*, *290*, 2519–2538.
Zhao, X. P., and J. T. Hoeksema (2010), The magnetic field at the inner boundary of the heliosphere around solar minimum, *Sol. Phys.*, *266*, 379–390.
Zhao, X. P., S. P. Plunkett, and W. Liu (2002), Determination of geometrical and kinematical properties of halo coronal mass ejections using the cone model, *J. Geophys. Res.*, *107*, 1223, doi:10.1029/2001JA009143.
Zhao, X. P., P. H. Scherrer, and J. T. Hoeksema (2004), The effect of the differential rotation of photospheric magnetic features on synoptic frames of the photospheric magnetic field, *Abstract #SH21B-0419 presented at 2004 Fall Meeting Abstracts*, AGU, San Francisco, Calif., 13–17 Dec.
Zhou, Y. F., and X. S. Feng (2013), MHD numerical study of the latitudinal deflection of coronal mass ejection, *J. Geophys. Res. Space Physics*, *118*, 6007–6018, doi:10.1002/2013JA018976.
Zhou, Y. F., X. S. Feng, and X. H. Zhao (2014), Using a 3-D MHD simulation to interpret propagation and evolution of a coronal mass ejection observed by multiple spacecraft: The 3 April 2010 event, *J. Geophys. Res. Space Physics*, *119*, 9321–9333, doi:10.1002/2014JA020347.
Zurbuchen, T. H., and I. G. Richardson (2006), In-situ solar wind and magnetic field signatures of interplanetary coronal mass ejections, *Space Sci. Rev.*, *123*, 31–43.